Macroscopic graphite felt containing palladium catalyst for liquid-phase hydrogenation of cinnamaldehyde

Zhenxin Xu[a,*], Cuong Duong-Viet[a,b], Yuefeng Liu[c], Walid Baaziz[d], Bing Li[a], Lam Nguyen-Dinh[e], Ovidiu Ersen[d], Cuong Pham-Huu[a,*]

[a] Institut de Chimie et Procédés pour l'Energie, l'Environnement et la Santé (ICPEES), ECPM, UMR 7515 du CNRS-Université de Strasbourg, 25 rue Becquerel, 67087 Strasbourg Cedex 02, France
[b] Ha-Noi University of Mining and Geology, 18 Pho Vien, Duc Thang, Bac Tu Liem, Ha-Noi, Viet Nam
[c] Dalian National Laboratory for Clean Energy (DNL), Dalian Institute of Chemical Physics, Chinese Academy of Science, 457 Zhongshan Road, 116023 Dalian, China
[d] Institut de Physique et Chimie des Matériaux de Strasbourg (IPCMS), UMR 7504 du CNRS-Université de Strasbourg, 23 rue du Loess, 67037 Strasbourg Cedex 08, France
[e] The University of Da-Nang, University of Science and Technology, 54, Nguyen Luong Bang, Da-Nang, Viet Nam

ARTICLE INFO

ABSTRACT

Developing of both effective and stable noble metal nanoparticle (NPs) catalysts with easy catalyst-product recovery is still challenging in the liquid-phase catalytic processes. Here, we report on the synthesis of a hierarchical structured catalyst that consisted of oxygen functionalized graphite felt (OGF) support for liquid-phase processes. The monolith palladium-based catalyst was used as catalytic stirrer and displays excellent stability as well as complete recyclability for liquid-phase hydrogenation of α, β-unsaturated cinnamaldehyde. The surface defects decorated with abundant oxygenated groups as well as highly accessible porous structure generated from the acid treatment of carbon support, construct a bridge between Pd and support providing the charge transfer to alter the metal-support interactions. The electron-deficient high-valent Pd$^{\delta\delta+}$ species, formed on the metal NPs, and defects on the support help to enhance the Pd dispersion and resistance to sintering and/or aggregation during both catalyst preparation and cycling tests, leading to the high and stable hydrogen dissociative adsorption for hydrogenation process.

1. Introduction

Catalytic processes represent an important part in the production of goods and chemical compounds for the everyday life in our society [1,2]. Numerous catalytic processes are conducted in liquid-phase medium where diffusion of gaseous/liquid reactants to the active site, localized on the solid catalyst surface, is several orders of magnitude higher than that occurs in the gas-phase processes. Such diffusion could significantly decrease the intrinsic activity of the catalyst and also modifies the overall selectivity of the process through secondary reaction. In addition, most of the liquid-phase catalysts are in powder form which calls for an efficient catalyst-product recovery step. Indeed, the powdered catalyst-product recovery represents an incentive process and catalyst loss is frequently encountered during the recovery process. Several attempts have been developed in order to facilitate the catalyst-products separation, i.e. magnetic support [3,4], basket containing catalyst and structured catalysts with nanoscopic carbon support coated on monolith or foam host matrix [5–8]. However, most of the structured systems, based on the use of monolith and foam, are constituted by relatively thick host matrix structure exceeding hundred micrometers or even more, which could hinder the diffusion of the reactant to the active phase localized inside the pores of the support. The tortuosity of the porous network also induces long apparent sojourn time which favors secondary reactions. Despite the advantages regarding the recovery step such structured catalysts still suffer from low catalytic performance due to the diffusion limitations. The development of new catalyst support with better performance represents another aspect for the improvement of the catalytic performance by providing adequate structure with high effective surface area, reduced diffusion limitations and low pressure drop. It significantly contributes to the selectivity of the process as well as to the long-term stability of the catalyst by reducing deactivation through poisoning by secondary products. For liquid-phase reactions the use of the structured catalysts instead of slurry ones allows the avoidance of the costly and time consuming filtration process to separate the catalyst from the final product [9]. Structured catalysts also prevent the problem of fine

---

* Corresponding authors.
E-mail addresses: zhenxin.xu@etu.unistra.fr (Z. Xu), cuong.pham-huu@unistra.fr (C. Pham-Huu).

formation as encountered with slurry reactor due to the attrition of small particles, consecutive to the repeated impacts between the catalyst particles and the stirrer, under vigorous stirring that leads to the plugging of filtration device. Finally, microturbulences generated inside the structured catalyst also contribute to a higher degree of reactant mixing leading to a better catalytic performance [10].

The development of carbon materials (CMs), especially carbon nanotubes/nanofibers and graphene, has drawn increasing attention from both scientific and industrial researchers operated in the heterogeneous catalysis processes [11–13]. Because of their high porous structure, excellent resistance to acid or basic media, remarkable electrical and thermal conductivity, especially facile recovery for loading metal by combustion, CMs used as heterogeneous catalyst supports play an essential role in the noble metal catalyzed liquid-phase reaction. However, for the noble metal catalyst deposited on the pristine CMs, the rapid deactivation with extremely weak cycling stability and the low selectivity of catalysts restrict their potential application, which are caused from the leaching out or the aggregation of metal nanoparticles (NPs) during the catalyst evaluation due to the low metal-support interaction [14,15]. It is demonstrated that these problems can be overcome by the modification of surface chemistry on the CMs with the introduction of oxygen-containing functional groups or heteroatoms (e.g., nitrogen, sulfur, phosphorus), which could reinforce the interaction between the carbon support and metal NPs or anchor the metal NPs on the carbon [16–20].

Commercial graphite felt (GF) constituted by entangled graphite filamentous with few micrometers in diameter displays high effective surface along with large voids (connected porosity), which could be of high interest for acting as catalyst support [21]. In addition, GF is widely produced for application in numerous fields such as filter for fume hood, insulation structure for high temperature ovens, sounds absorber, etc. However, commercial GF when used as catalyst support display several drawbacks: low specific surface area for dispersing of the active phase, hydrophobic character which prevents the anchoring of the active phase and low metal (oxide)/support interaction for preventing excessive sintering of metal NPs during the catalytic process. GF composites decorated with a layer of carbon nanofibers, growth through the Chemical Vapor deposition (CVD) method using nickel as growth catalyst, have been developed for being used as catalyst support with high dispersion properties along with strong interaction to prevent excessive metal sintering [22]. However, such composites require the use of metal catalyst for the growth of carbon nanofibers as well as relatively high temperature synthesis process in the presence of explosive gaseous reactants, i.e. hydrocarbons and hydrogen, and a tedious purification process to remove the growth catalyst [23,24]. It is of high interest to develop new synthesis method to functionalize the readiness commercial GF surface in order to improve the metal nanoparticles dispersion as well as the reduction of active phase sintering during the catalytic and regeneration processes if any. The method should be simple and easy for scaling up in order to facilitate the industrial development while the support should be robust enough for facing harsh reaction conditions to reduce the frequent replacement of the catalyst. The catalyst should also display controlled macroscopic shape, i.e. hierarchical structured catalysts, which could facilitate the catalyst-products recovery after the test [9].

The present work reports on the use of gaseous acid treated commercial GF as support for anchoring palladium NPs and it use as catalyst in the liquid-phase hydrogenation of α, β-unsaturated compounds. The GF is constituted by micrometers graphite filamentous with open structure (90% of voidage), which will significantly reduce the diffusion path of the reactant towards the active phase. The acid treatment was carried out under gaseous nitric acid at medium temperature leading to the formation of a micro- and mesoporous carbon structure, especially localized on or near the graphite surface, with a high specific surface area, accessible porosity along with oxygenated functional groups decorating defects on the surface. The oxygenated groups and the

defects provide strong anchorage sites for dispersing palladium particles while the lack of ink-bottled pores significantly improve the diffusion rate allowing the maintenance of a high hydrogenation activity along with high selectivity. The as-synthesized GF-based catalyst is subsequently used as catalyst stirrer for liquid-phase hydrogenation process which allows one to phase out the costly filtration step to recover the catalyst from the reactant mixture.

2. Experimental section

2.1. Materials and catalysts

The commercial GF constituted by carbon microfilamentous (Carbone Lorraine Ltd) were firstly treated by gaseous HNO_3 as reported previous (Figure S1) [25,26]. In a typical procedure, the GF in the form of disk (∅ x thickness of 24 × 6 mm, 0.24 g) was loaded in a tubular reactor which was connected to a round bottom flask filled with 10 mL of HNO_3 (65%). The round bottom flask with HNO_3 solution was heated at 125 °C and keep under magnetic stirring. Meanwhile the 10 mL/min of Ar was introduced into the flask to drive the gaseous acid upwards through the GF. The GF sample was treated in the presence of gaseous acid at 250 °C for 4 h. The reactant gas passed through the GF bed was further condensed in another flask. The pressure of the treatment system is 1 atm. The as-treated sample was then washed once with deionized water to remove trace amount of impurities followed by an oven drying at 130 °C overnight. The as-treated GF were denoted as OGF.

The palladium was deposited onto the carbon support via an incipient wetness impregnation method using a palladium nitrate (Pd$(NO_3)_2$·6H$_2$O, Fluka) as salt precursor in aqueous solution. The theoretical concentration of metallic Pd was fixed at 5 wt. %. The impregnated solid was oven dried at 110 °C for 2 h and calcined in air at 350 °C for 2 h in order to decompose the palladium nitrate into its corresponding oxide. The catalyst was further reduced under hydrogen flow at 350 °C for 2 h. The catalyst was removed from the reactor at room temperature and stored in close vial before characterizations or catalytic experiments.

2.2. Hydrogenation performance

The selective hydrogenation of cinnamaldehyde (CAD) led to the formation of three reaction products namely hydrocinnamaldehyde (HCAD), which was formed by the selective hydrogenation of the C═C bond, cinnamyl alcohol (CAL), which was formed by the selective hydrogenation of the C═O bond, and hydrocinnamylalcohol (HCAL) which was formed by a complete hydrogenation of both unsatured C═C and C═O bonds (Figure S2). The selective hydrogenation of the CAD was carried out in a glass reactor (volume = 250 mL) at atmospheric pressure. The Pd/GF catalyst was mounted on a glass holder fixed to a mechanical stirrer and thus, acting both as a catalyst and as mechanical stirrer. Work is ongoing to evaluate the influence of the other stirrer-catalyst configuration such as those reported by Schouten and co-workers [27], i.e. T-shaped stirrer, on the hydrogenation performance. The reaction medium contains different concentrations of CAD diluted in a dioxane solvent (100 mL) and was heated up from room temperature to the reaction temperature (80 °C) with an oil bath with a heating rate of 5 °C/min. Dioxane was used instead of alcohol in order to avoid any homogeneous reactions which could lead to the formation of heavier by-products. At 80 °C the catalyst was immersed into the reaction medium and rotated at different speeds (250–500 rpm).The hydrogen was continuously supplied into the reactor medium at a flow rate of 50 mL/min. The hydrogen stream was regulated by Brooks 5850 TR mass flow controller. The liquid medium was withdrawn at a regular time and analyzed by a gas chromatography (GC) on a Varian 3800 CX equipped with a PONA column and a Flame Ionization Detector (FID). The products were calibrated by using pure

components diluted in a dioxane solution. The conversion and product distribution were calculated from the GC results.

2.3. Characterization techniques

The morphology of the composite was characterized by scanning electron microscopy (SEM) on a JEOL F2600 microscope equipped with a CCD camera. The sample was covered with a thin layer of gold before analysis in order to avoid the problem of charging effects.

The microstructure of the carbon filamentous and the deposited metal active phase was analyzed by transmission electron microscopy (TEM). The TEM analyze was carried out on a JEOL 2100 F working at 200 kV accelerated voltage and a point-to-point resolution of 0.1 nm. The sample was dispersed by ultrasounds in an ethanol solution for 5 min and a drop of the solution was deposited on a copper grid covered with a holey carbon membrane for observation.

The Raman spectra were recorded using a LabRAM ARAMIS Horiba Raman spectrometer equipped with a Peltier cooled CCD detector. A laser line (532 nm/100 mW (YAG) with Laser Quantum MPC600 PSU) was used to excite sample.

BET surface areas were measured using a commercial BET unit (Tristar, Micromeritics) using N_2 adsorption at 77 K. Before the N_2 adsorption, samples were heated at 300∘C for 3 h under dynamic vacuum to desorb surface impurities. S_{BET} is the surface area of the sample calculated from the nitrogen isotherm using the BET method. The pore size distribution was determined from the results obtained on the desorption branch of the N_2 isotherm.

The oxygen functional groups of samples were determined by the temperature-programmed desorption conducted on a Micromeritics ASAP-2100 setup equipped with a multichannel mass spectrometer. In a typical procedure, 50 mg of the samples was loaded in the reactor and then flushed with He (50 mL/min) at 50 °C for 1 h. Afterward, the temperature was raised from 50 to 1000 °C at a heating rate of 5 °C/min. The evolved species were monitored with intensities of m/e 28 (CO) and 44 (CO_2), respectively.

The temperature-programmed reduction of hydrogen (H_2-TPR) was conducted on a Micromeritics ASAP-2100 setup equipped with a multichannel mass spectrometer. In a typical procedure, 50 mg of the sample was previously heated for 1 h at 130 °C under an Ar stream, and then it was cooled to room temperature. After the stream was switched from Ar to 10% H_2/Ar mixture gas flow of 50 mL/min, the sample was heated by increasing the temperature linearly at a rate of 10 °C/min. The evolved species were monitored with intensities of m/e 2 (H_2).

The X-ray photoelectron spectroscopy (XPS) was performed on a MULTILAB 2000 (THERMO) spectrometer equipped with an Al Kα X-ray source (1486.6 eV) with 10 min of acquisition to achieve a good signal to noise ratio. The C1s photoelectron binding energy was set at 284.6 eV relative to the Fermi level and used as reference to calibrate the other peak positions.

The temperature-programmed desorption of hydrogen (H_2-TPD) was conducted on a Micromeritics ASAP-2100 setup equipped with a multichannel mass spectrometer. In a typical procedure, 50 mg of the sample was reduced under 10% H_2/Ar mixture gas flow of 50 mL/min at 350 °C for 1 h before experiment. And then the temperature of sample was kept at 50 °C under 10% H_2/Ar mixture gas flow for 1 h. The He was switched in with a flow rate of 50 mL/min and the sample was flushed at 50 °C for 1 h. Afterward, the temperature was raised from 50 to 800 °C at a heating rate of 10 °C/min. The evolved species were monitored with intensities of m/e 2 (H_2).

3. Results and discussion

3.1. GF and OGF materials

The monolithic GF can be prepared with different macroscopic shapes depending to the downstream catalytic processes as presented in

Fig. 1A. The SEM micrographs (Figure S3) of the pristine carbon GF and the same after oxygen functionalization (OGF), through gaseous HNO_3 treatment at 250 °C for 4 h, indicated that the gross morphology of the structured carbon was retained after the oxidation treatment despite some mass loss due to oxidation (see discussion below).

The gaseous acid treatment induces a significant increase of the OGF specific surface area (SSA) compared to that of the pristine GF. As shown in Fig. 1B, the N_2 adsorption-desorption isotherm of GF and Pd/GF displayed the negligible adsorption of N_2, indicating the very little surface area without any porous structure. On the other hand, the isotherm of OGF and Pd/OGF exhibited the type IV isotherm curves with H4-type hysteresis loops according to the IUPAC classification, which signified the presence of capillary condensation in the mesoporous structure and the narrow slit-shaped pores [28]. Indeed, the HNO_3 treated sample (OGF) displayed a SSA of 168 m^2/g compared to 4 m^2/g for the pristine GF. Such large SSA increases could be directly attributed to the formation of pores or defects within the pristine GF during the oxidation process according to the TEM analysis presented below. The pore size distribution (inset of Fig. 1B) clearly evidences the formation of micro- and mesopores inside the oxidized GF which is expected to be at the origin of the SSA increase. It is worthy to note that the porosity formation did not alter the macroscopic shape of the material according to the SEM analysis presented above as a whole part of the pristine carbon microfilamentous was retained after the oxidation treatment despite some mass loss inherent to the oxidation process. Indeed, the defects and oxygen functionalization were carried out through oxidation of the pristine GF during the process which resulted to an increase of the SSA and also a mass loss accounted for about 13 wt. % [26,27].

Raman spectroscopy was performed to investigate the change in the graphitic structure of GF after the oxidation process. As shown in Fig. 1C, both GF and OGF fitted three bands corresponding to the different carbonaceous structures: the G band attributed to an ideal graphitic lattice at around 1580 cm^{-1}, the D band (∼1350 cm^{-1}) associated with the structural defects and D' band corresponding to the disordered graphitic fragments at ∼1620 cm^{-1}, respectively [29,30]. After the oxidation process, the I_D/I_G increased from 0.77 for GF to 1.95 for OGF while the I_D/I_G increased more than 3 times from 0.26 to 0.84. Such results indicated that the gaseous oxidant treatment significantly modified the graphitic lattice of GF by creating more defects and disordered graphitic fragments inside the sample. Moreover, the G band of treated OGF shifted to the higher wavenumber by about 12 cm^{-1} compared to that of GF, which may be attributed to the presence of oxygen-containing functional groups generated on the surface [31].

The surface oxygen groups present on GF and OGF were characterized by TPD-MS and the results are presented in Fig. 1D and E. The oxygen functional groups are decomposed according to the evolution of CO_2 (originated from carboxylic acids, anhydrides and lactones) or/and CO (originated from anhydrides, phenols and carbonyls) at different temperatures [32,33]. The total amounts of CO_2 and CO released and surface oxygen contents were calculated from the corresponding TPD spectra (Table 1). The TPD results indicated that there were extremely few oxygen groups on the surface of the pristine GF which is in good agreement with the hydrophobic character of the material. After the oxidation treatment in the presence of gaseous HNO_3 at 250 °C for 4 h, the amount of surface oxygen functional groups increased more than 18 times for OGF according to the TPD experiments. Furthermore, the oxidation treatment also introduces hydrophilicity to the composite as shown in Fig. 1F where untreated GF remains on top of the water medium while the treated, OGF, steadily sinks to the bottom, which is due to the incorporation of oxygenated functional groups on the defects or surface of the treated sample. [34]

TEM analysis is used to investigate the influence of oxidation treatment on the microstructure of GF. As displayed in Fig. 2, the pristine GF is composed of ordered graphitic layers with very little pore on the surface which is in good agreement with it low SSA. After the
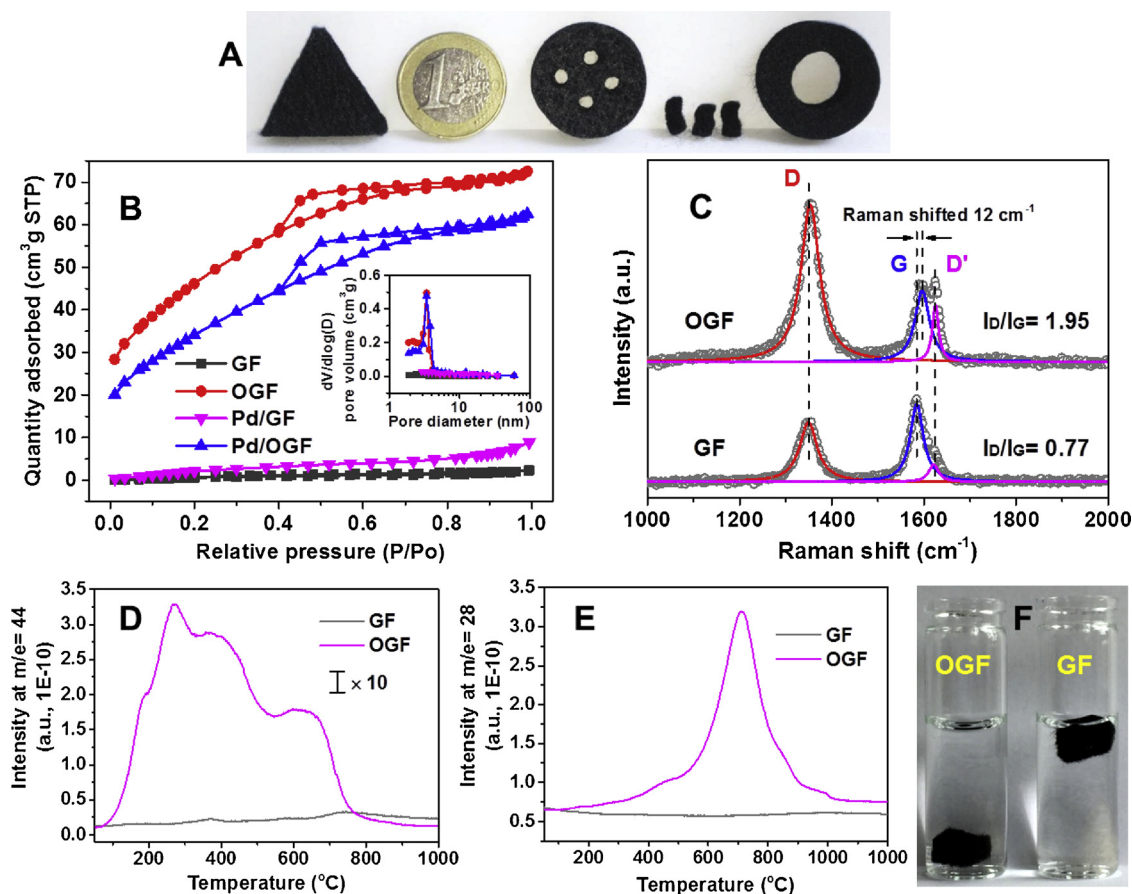
Fig. 1. (A) Digital photo of the GF with different macroscopic shaping. The macroscopic shapes were completely retained after the acid treatment while a mass loss of ca. 13 wt.% was observed. (B) N_2 adsorption/desorption isotherms and pore size distributions (inset) of the pristine GF, OGF, Pd/GF and Pd/OGF. (C) Raman spectra, (D) CO_2 ($m/z = 44$) and (E) CO ($m/z = 28$) generated during the TPD analysis of the GF and OGF. (F) Digital photo of samples in water showing the surface character change before (GF) and after acid (OGF) treatment.

Table 1
Surface oxygen determined by TPD-MS (in the form of CO and CO_2).

Sample	CO	CO_2	Surface oxygen contents	
	(μmol/g)	(μmol/g)	(μmol/g)	(wt %)
GF	107	29	165	0.26
OGF	2423	280	2983	4.77

gaseous acid treatment, TEM analysis evidences the formation of a highly porous carbon structure on the outer region of the fiber of OGF (pointed out by arrows in Fig. 2C and D).

According to the TEM analysis the dense carbon structure of the GF was converted into a highly porous carbon structure with a large number of pores. It is expected that during the treatment to generate such highly porous carbon a large number of surface defects was also formed. This is in good agreement with the previous analysis of N_2 adsorption-desorption isotherm which clearly suggests the significant increased SSA on OGF. Such structure is expected to be formed through oxidation of a weakly graphitized carbon by the gaseous HNO_3 during the treatment, which leaving behind entangled carbon structure with high oxygenated decorating defects according to the Raman and TPD results presented above. Additional investigation will be made using TEM in tomography mode (TEM-3D) [35] which will allow one to get access to the porosity distribution of the sample and the localization of the metal nanoparticles with respect to such porosity. The results reported above confirmed that the gaseous HNO_3 thermal oxidation process is an efficient method for the synthesis of high SSA carbon

materials containing structural defects decorated with oxygenated functional groups as well as porous architecture.

3.2. Pd/OGF characteristics

The profiles of H_2-TPR equipped with mass spectrometer for the supported Pd catalysts are shown in Figure S4. The sharp positive peak that appears in both of samples can be attributed to the H_2 release due to the decomposition of Pd hydride. [36] The absence of any H_2 consumption (negative peak) preceding hydride decomposition suggests the formation of zero-valent Pd at room temperature. The hydride decomposition temperature of Pd/OGF (88 °C) is lower than that recorded of Pd/GF (96 °C), indicating the smaller Pd particle size in Pd/OGF. [37] Moreover, there is no any H_2 consumption in Pd/GF, suggesting the complete reduction of sample at room temperature. Notably, the evolution of H_2 in Pd/OGF is accompanied by appreciable negative H_2 consumption peak around 122 °C, which can be attributed to the reduction of palladium species that interact with the support more strongly. [38]

XPS was conducted to perform surface elemental analysis of the catalyst, including the metal dispersion and the impact of support on the electronic structure of Pd phase via metal-support interactions. The Pd3d XPS spectra of catalysts (Fig. 3A) present two main peaks at about 335.2 and 340.5 eV, corresponding to the doublet of Pd $3d_{5/2}$ and $3d_{3/2}$, respectively. In agreement with the literature, the deconvolution of core level Pd$3d_{5/2}$ reveals the presence of predominant metallic phase (Pd^0, 335.0 eV), oxide state metal (Pd^{2+}, 337.2 eV) and a satellite peak (338.4 eV). [39,40] There is an additional prominent signal (336.0 eV)
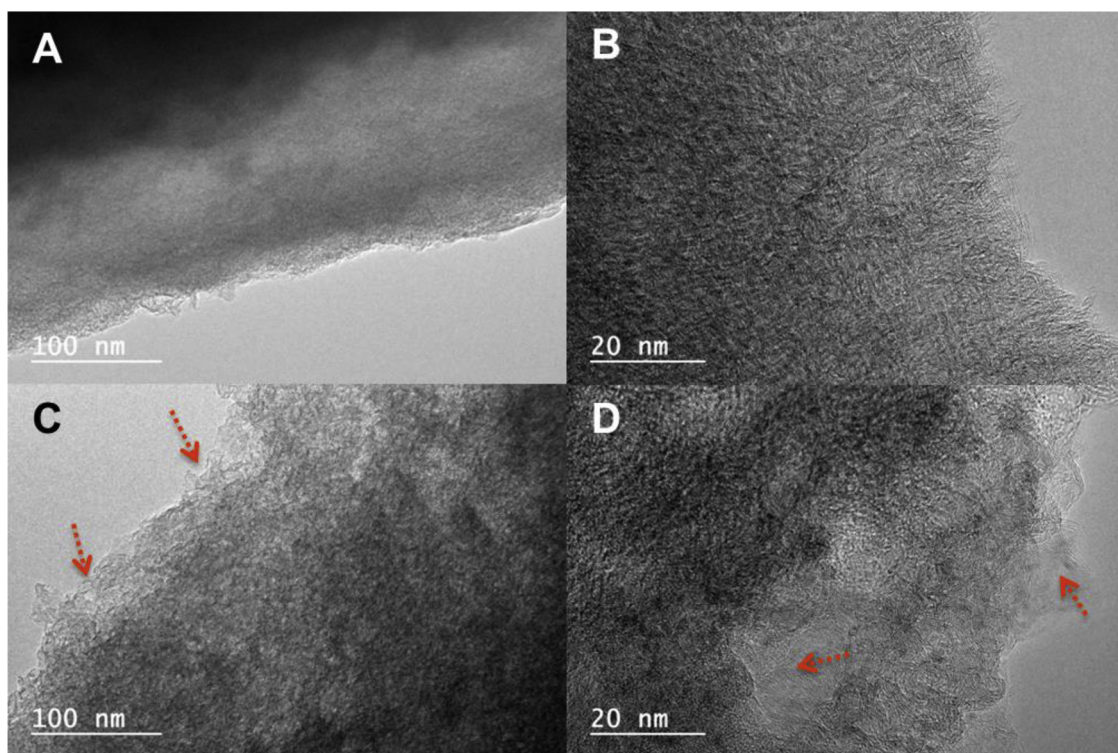
Fig. 2. TEM images of the pristine GF (A, B) and OGF (C, D). The porous microstructure generated after the oxidation treatment inside the OGF is highlighted by arrows.
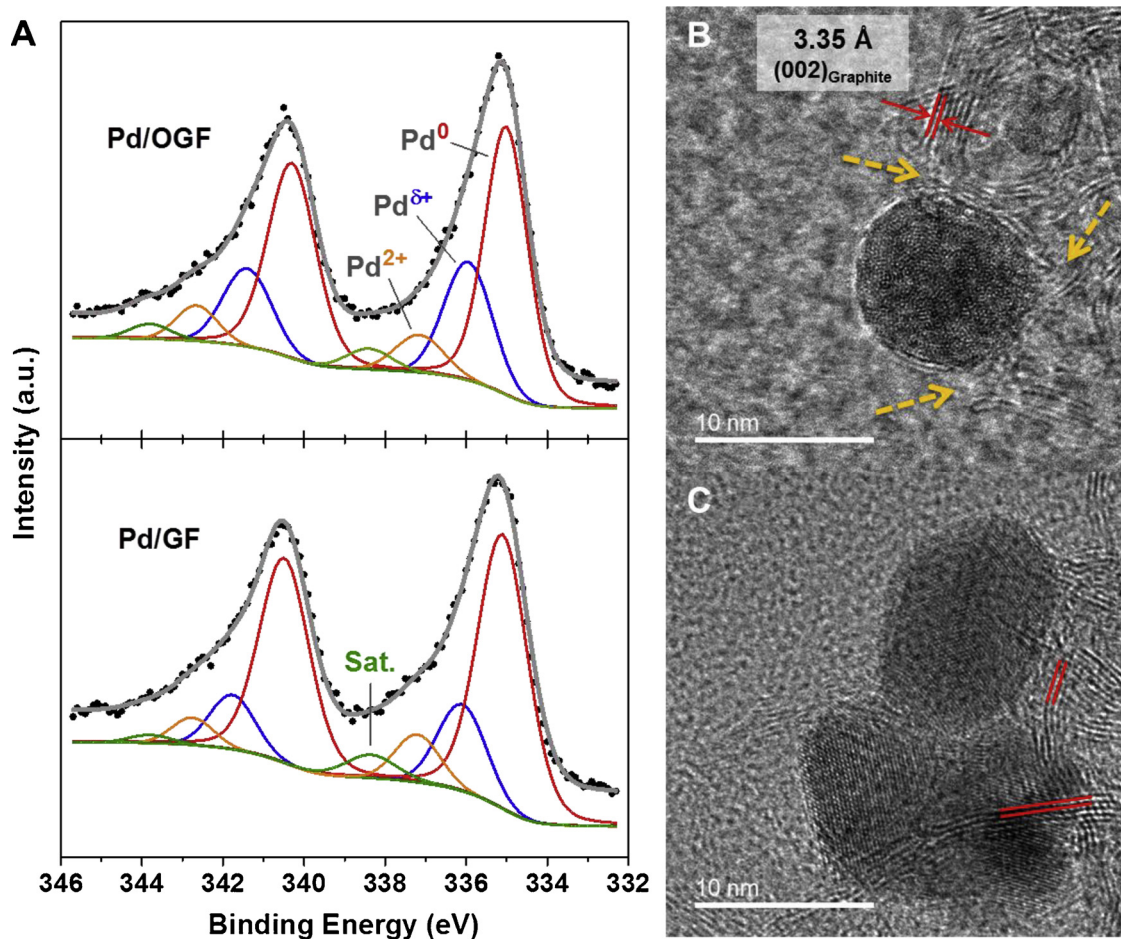

Fig. 3. (A) XPS Pd 3d spectra of reduced catalysts and high resolution TEM micrographs for (B) Pd/OGF and (C) Pd/GF.

Table 2
Pd elemental analysis and metal particle sizes of the samples.

Sample	Pd loading (wt%)	Percentage of peak area (%)				Pd at%[a]	Pd particle sizes[b] (nm)	
		Pd^0	$Pd^{\delta+}$	Pd^{2+}	Sat.		Reduced	Spent
Pd/GF	4.3	73.1	15.1	7.5	4.3	2.7	> 13.5	> 42.5
Pd/OGF	4.6	61.6	25.4	8.8	4.2	3.6	3.8 ± 0.8	3.8 ± 1.1

[a] The atom percent of surface Pd elemental on the catalysts determined from the XPS survey spectra.

[b] Pd particle sizes of reduced and spent samples determined by TEM analysis.

between Pd^0 and Pd^{2+}, which is ~1.0 eV higher than bulk Pd, suggesting electron transfer from Pd to the carbon support, resulting in electron-deficient metal atoms ($Pd^{\delta\delta+}$). The percentage of each peak as well as the atom percent of surface Pd on the catalyst, determined from the XPS survey spectra, are shown in Table 2. The oxide state Pd^{2+}, which was ascribed to the formation of Pd oxides upon sample storage in air, accounted for very little part in all Pd species. Interestingly, in this work, the proportion of $Pd^{\delta\delta+}$ in GF supported Pd increased after the oxidization of the carbon carrier, indicating a direct correlation between support properties and electronic characters of the Pd phase. These metal-support interactions are crucial to catalytic performance because they further improve the metal dispersion and thermal stability. Moreover, under the similarity of Pd loading amounts in two samples, the higher atom percent for surface Pd on Pd/OGF demonstrated that the oxidation process enriches the dispersion of Pd species on the surface of GF support (Table 2).

Some other groups have also reported the presence of $Pd^{\delta\delta+}$ phase in the carbon supported palladium catalysts, and linked these findings to the existence of metal-support interactions or electronic transfer associated with residual surface Cl [41–43]. Besides the experimental results [44,45], the theoretical calculations have also indicated that the electron transfer may occur between the carbon and the supported metal, including Pd, Pt, Ru and Ni [46–49]. The bonds between metal and carbon atoms can be formed at metal-carbon interface, thus providing an efficient link for charge transfer [50]. The transfer orientation could be considered by using the simple descriptors, such as electronegativity, which is commonly used in solid-state physics/chemistry [51–53]. The difference in electronegativity between palladium (2.20) and carbon (2.55) leads to the electron transfer from Pd NPs to carbon support at Pd-C interface. Furthermore, due to the much bigger electronegativity of oxygen (3.44), the oxidized carbon support, which is decorated with abundant oxygen functional groups at or near to the defects, would have a stronger tendency to attract more electrons from Pd NPs than untreated support. By density functional theory calculations, the charge transfer from Pd to graphene at graphene-Pd interface was confirmed in the system of monolayer graphene on Pd (111) [46]. Moreover, the interaction energies for Pd clusters on oxidized graphene are higher than those on a pure graphene support, indicating a significantly stronger interaction between the metal and the functionalized carbon support [39]. These results corroborate the Pd3d XPS data (Fig. 3A and Table 2) and suggest the high proportion of $Pd^{\delta\delta+}$ along with the strong metal-support interaction in Pd/OGF catalyst.

In order to understand the origin of the additional $Pd^{\delta\delta+}$ contribution in the XPS analysis from the morphology, high-resolution TEM of Pd/OGF and Pd/GF are displayed in Fig. 3B and C. In contrast to the majority of straight and ordered graphitic layers at the Pd-C interface in Pd/GF (Fig. 3C), the Pd NPs in Pd/OGF interface (Fig. 3B) follows more broken and curved carbon layers, suggesting that most of them bind to the structural defects decorated with oxygenated functional groups (pointed out by arrows in Fig. 3B), as well as the charge transfer at Pd-C interface can be induced by the oxygen functionalization of carbon support.

The Pd particle size distribution on both GF and OGF was investigated by means of TEM and the corresponding results are presented in Fig. 4. According to the low magnification TEM analysis the

Pd particles are smaller and homogeneous in size in the Pd/OGF catalyst compared to that deposited on the untreated Pd/GF (Fig. 4A–B and D–E). High resolution TEM micrographs (Fig. 4C and F) confirm the high dispersion of the palladium nanoparticles with extremely homogeneous in size on the Pd/OGF sample compared to that of the Pd/GF, which could be directly attributed to the strong interaction between the metal NPs with the defective carbon support surface. On the other hand, TEM analysis reveals much lower palladium particles dispersion on the untreated support which is in good agreement with the preceding XPS analysis. It is also worthy to note that the Pd NPs are well separate from each other in the Pd/OGF sample with an almost absence of aggregate (Fig. 4F) while they are presence in the form of large aggregates on the Pd/GF (Fig. 4C) which pointed out the existence of a strong metal-support interactions with the defective carbon support. The particle size distribution of the Pd NPs, determined from more than 200 particles, is relatively narrow and centered at around 4 nm (Inset of Fig. 4F).

H_2-TPD was also conducted for the analysis of metal dispersion (Figure S5), the peak area of desorbed H_2 on Pd/OGF is much larger than that on Pd/GF, indicating that not only the higher dispersion of the Pd NPs, but also the stronger hydrogen uptake capacity of Pd/OGF, which is an important consideration in H_2-mediated liquid-phase catalysis where the H_2 dissociation on the catalyst surface is a rate limiting step (see discussion below on the influence of H_2 concentration on the hydrogenation performance). Such results pointed out the importance of structural and functionalization properties of carbon support for obtaining high and stable metal NPs dispersion under elevated temperature reduction during catalyst preparation.

Based on the result and discussion above, the oxygen functionalization of GF by gaseous HNO_3 thermal treatment generates a unique architecture consist of abundant oxygenated groups decorated structural defects as well as porous structure with high exposure surface area. The high specific surface area of OGF provides a large Pd-support interface which significantly improve the metal dispersion. [54] Meanwhile the oxygen-rich functional groups have great potential as electron acceptors which could provide anchorage sites for the metal NPs [55,56]. Combined with the modification of support electronic property from the structural defects, the oxygen functionalization in OGF induces the charge transfer from Pd atom to carbon support at metal-C interface, giving rise to a Strong Metal-Support Interaction (SMSI) in Pd/OGF associated with the high performance of high dispersed Pd NPs with good thermal stability.

3.3. Catalytic performance

The liquid-phase hydrogenation of cinnamaldehyde using such structured catalyst as catalytic stirrer was conducted under different reaction conditions, i.e. stirring speed, initial CAD concentration, reaction temperature and hydrogen flow rate, to evaluate the catalytic performance between monolithic pristine GF and oxidative OGF supported Pd catalysts.

3.3.1. Influence of stirring speed

The hydrogenation reaction was carried out at 80 °C with different stirring speed ranged between 250 and 500 rpm. The catalytic results,
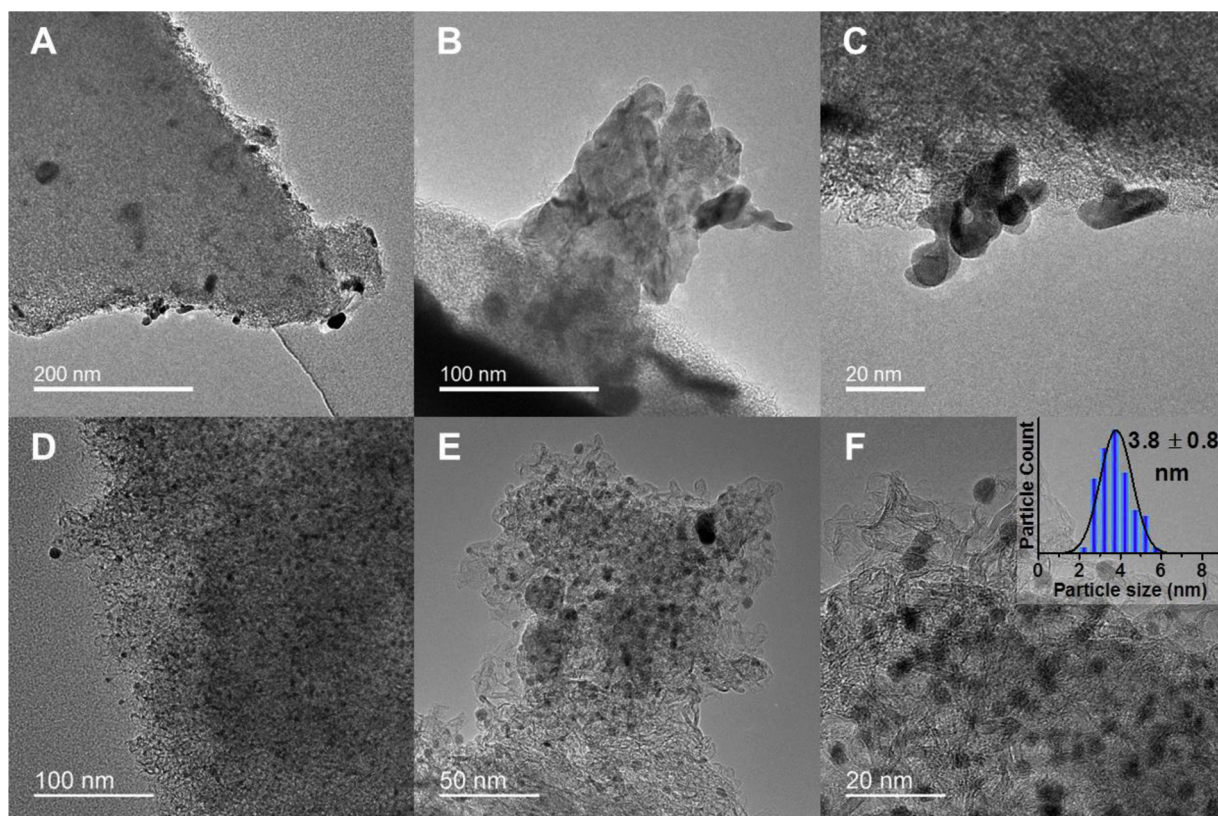
Fig. 4. TEM micrographs of the Pd/GF (A, B and C) and Pd/OGF (E, E and F) catalysts after reduction and before reaction. Inset of (F): Pd particle size distribution determined from.
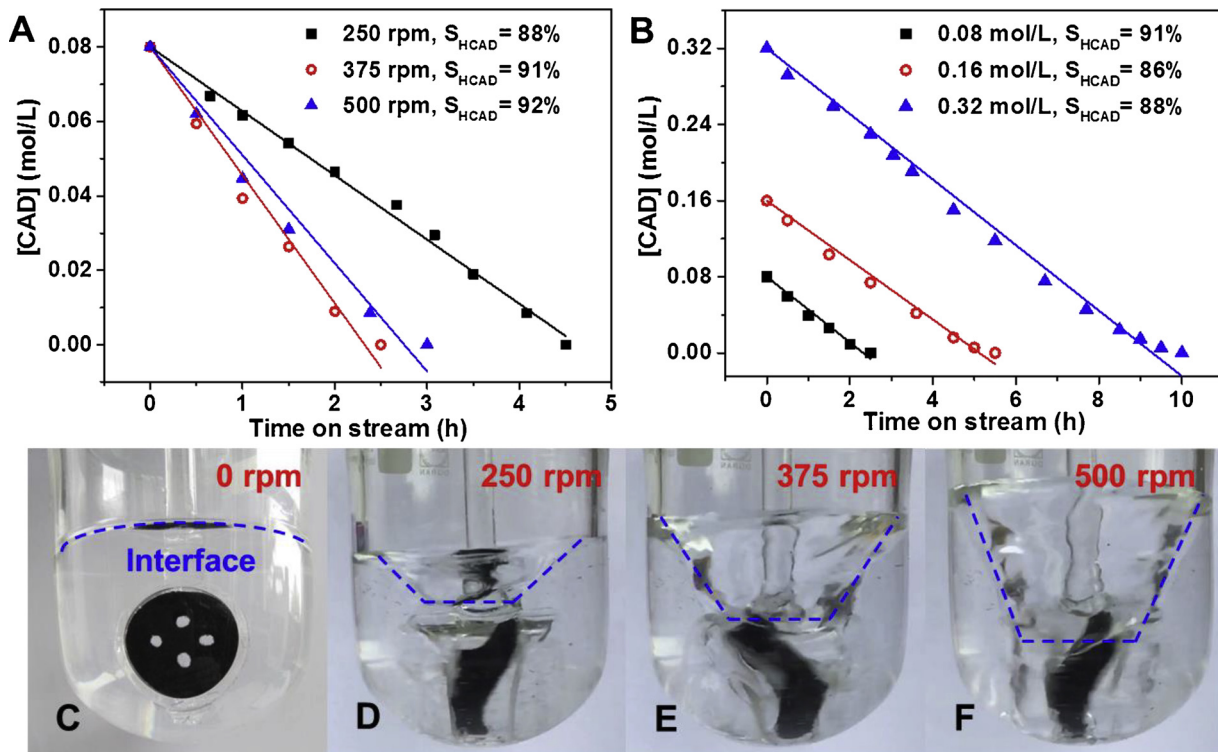

Fig. 5. Influence of the reaction parameters on the C=C bond hydrogenation on the Pd/OGFs catalyst: (A) stirring rate and (B) cinnamaldehyde concentration. (C–F) Digital photo of the reactor using catalytic stirrer with different stirring rate. Reference conditions: 50 mL/min H_2, 80 °C, 1 atm, 375 rpm and 0.08 mol/L of CAD.

expressed in terms of CAD concentration, mol/L, as a function of time-on-stream (TOS) are presented in Fig. 5A. The hydrogenation activity increases and reaches a maximum rate at 375 rpm while it slightly decreases at higher stirring rate, i.e. 500 rpm (Fig. 5A). The deviation of the cinnamaldehyde conversion at the end of the test could be attributed to the depletion of CAD in the medium and thus, inducing a CAD gradient concentration in the liquid medium which slower the adsorption rate of CAD on the catalyst surface. The influence of the stirring rate on the activity has already been reported by Tschentscher et al. for the oxygen/water system with rotating foam catalyst and could be explained by the contacting mode between liquid and stirrer during mixing process. [57] As shown in Fig. 5C-F, the liquid would rotate following the rotated stirrer, and then the strong centrifugal force from high stirring speed could make the liquid reactant accumulate close to the wall of the reactor with descending liquid interface and then far away from the center of stirrer [58]. Under this situation, the reactant could not effectively contact the middle of the catalyst. On the other hand, high rate of agitation might cause the swirling flow, which further destroyed the micro-mixing. Therefore, the high rotating speed brought the loss of catalytic activity. For the subsequence tests, a stirring speed of 375 rpm will be used unless specified.

The selectivity of the C═C bond hydrogenation product slightly increases as a function of the stirring speed and remains almost unchanged between 375 and 500 rpm. The increase of the C═C bond hydrogenation selectivity from 250 to 375 rpm could be attributed to the rapid refreshment of the liquid layer on the catalyst surface which contributes to a higher desorption rate of the intermediate product before secondary hydrogenation occurs. Similar results have already been reported previously [59]. The refreshment seems to attaining a limit at higher stirring speed, due to the problem of liquid/catalyst contact as discussed above, and only a marginally improvement of the C═C bond hydrogenation was observed.

3.3.2. Influence of initial CAD concentration

The catalytic results, expressed in terms of CAD concentration, mol/L, obtained at 80 °C with different initial CAD concentrations are presented in Fig. 5B as a function of time-on-stream (TOS). According to the results the C═C bond hydrogenation performance is almost proportional to the CAD concentration which confirm that the diffusion is not the limiting steps for the reaction at atmospheric pressure. Such results could be explained by the highly porous and micrometric dimension of the carbon filamentous and also to the lack of inner porosity of the support which significantly increase the reactant diffusion towards the active sites. The fact of using the catalyst as stirrer also provides faster reactant refreshment on the catalyst surface which could contribute to such results. The CAD initial concentration does not modify in a significant manner the C═C bond hydrogenation selectivity which remains between 86 and 91% taken into account experimental errors consecutive to the GC analysis.

3.3.3. Influence of the reaction temperature

The influence of the reaction temperature was evaluated between 40 and 80 °C and under atmospheric pressure. The stirring rate was keep at the most efficient value of 375 rpm. The CAD conversion was almost double when increasing the reaction temperature from 40 °C to 80 °C along with the increased C═C bond hydrogenation selectivity (Fig. 6A). Such results indicate that secondary reaction, i.e. complete hydrogenation, is not favored by medium reaction temperature on the Pd/OGF catalyst. It seems that the intermediate hydrogenated product is steadily desorbed from the catalyst surface before complete hydrogenation occurs while re-adsorption is unlikely to occur regardless the reaction temperature. Again, the C═C bond hydrogenation selectivity remains between 88 and 91% which indicates that at such reaction temperature almost no additional secondary reaction was expected.

3.3.4. Influence of the hydrogen flow rate

In the hydrogenation process the ability of the catalyst to dissociate hydrogen is primordial and the high dissociative adsorption of hydrogen allows the reduction of hydrogen in both inlet and exit stream which could be of high interest for recycling step. For comparison, the reaction is carried out on both Pd/OGF and Pd/GF catalysts, with different palladium dispersions according to the TEM analysis reported above, under similar reaction conditions, i.e. [CAD] = 0.08 mol/L and H$_2$ flow rate of 50 mL/min. According to the results presented in Fig. 6B the two catalysts display a similar activity. In light of the results one can conclude that, at low CAD concentration and relatively high H$_2$ flow rate, dissociative adsorbed hydrogen on the catalyst surface on both high and low metal dispersion catalysts is largely sufficient for performing the hydrogenation of the CAD on the catalysts surface.

The catalytic hydrogenation performance of the Pd/OGF catalyst was evaluated under a more severe reaction conditions, i.e. CAD concentration of 0.32 mol/L and atmospheric pressure with various H$_2$ flow rate (Fig. 6C). According to the results the time for complete conversion of CAD slightly increased about 10% when the H$_2$ flow rate was decreased from 50 mL/min to 12.5 mL/min which confirms that on the Pd/OGF catalyst, with high palladium dispersion, the hydrogen dissociative adsorption on the Pd NPs under lower H$_2$ flow rate hardly influences the hydrogenation activity, despite in the presence of a higher CAD on the catalyst surface due to the increase of CAD concentration in the reaction medium. It seems that the rate of hydrogen dissociative adsorption on the small palladium particles of the Pd/OGF is high and provides enough adsorbed hydrogen to convert the adsorbed CAD on the catalyst surface.

In order to verify such assumption the same reaction was carried out on both catalysts under severe reaction conditions: [CAD] = 0.32 mol/L and H$_2$ flow rate = 12.5 mL/min. Under these reaction conditions the hydrogenation rate obtained on the Pd/OGF is much higher, i.e. more than twice, than the one obtained on the Pd/GF catalyst according to the results presented in Fig. 6D whereas the hydrogenation rate is similar between the two catalysts at high hydrogen flow rate and at low CAD concentration as shown in Fig. 6B. It is expected that on the Pd/GF with lower palladium dispersion, and as a consequence of larger palladium particle size, the rate of hydrogen dissociation seems to be much slower at low hydrogen flow rate leading to an insufficient adsorbed hydrogen for the complete hydrogenation of the adsorbed CAD on the catalyst surface, and resulting thus to a lower hydrogenation performance. Such results indicate that acid treatment allows one to produce OGF support with high dispersion properties for metal which, in turn, leads to a highly active catalyst for operating under severe reaction conditions.

The selectivity towards the C═C bond hydrogenation remains almost unchanged which indicates that consecutive reaction leading to complete hydrogenated product is not depending on the amount of adsorbed hydrogen at the catalyst surface but only on the desorption rate of the intermediate product.

3.3.5. Catalyst stability as a function of cycling tests

Catalyst deactivation as a function of cycling tests is the most common observed trend in heterogeneous liquid-phase processes due to several factors such as active phase loss consecutive to leaching or fine formation, catalyst loss during the recovery step and also to sintering. In this section the stability behavior of the Pd/OGF, Pd/GF and commercial Pd/AC (Pd/activated charcoal provided by Sigma-Aldrich) catalysts was evaluated. The weight amount of the catalyst was adjusted in order to have the same metal active phase weight for the comparison tests. The cycling tests were carried out as follow: for the catalytic stirrers (Pd/GF and Pd/OGF), after reaction the liquid was removed and the reactor was filled with 100 mL of dioxane, the catalyst was stirred at 375 rpm for 30 min in order to desorb the adsorbed products on its surface or inside the porosity; for the commercial Pd/AC catalyst the powdered catalyst was allowed to settle down before
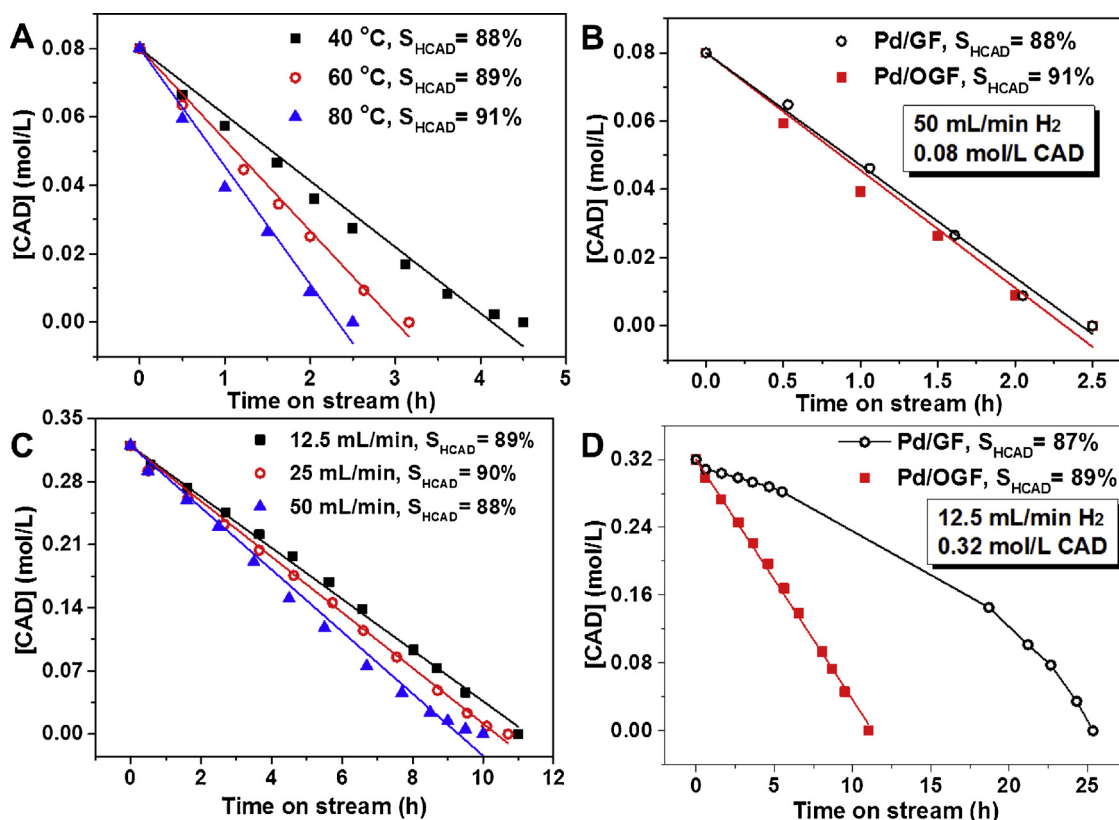
Fig. 6. (A) Influence of the reaction temperature, (B) Cinnamaldehyde conversion as a function of the hydrogen flow rate on the Pd/OGF catalyst, (C and D) Cinnamaldehyde conversion as a function of the adverse cinnamaldehyde concentration to hydrogen flow rate on Pd/OGF and Pd/GF catalysts. Reference conditions: 50 mL/min H_2, 80 °C, 1 atm, 375 rpm, and 0.08 mol/L of CAD.
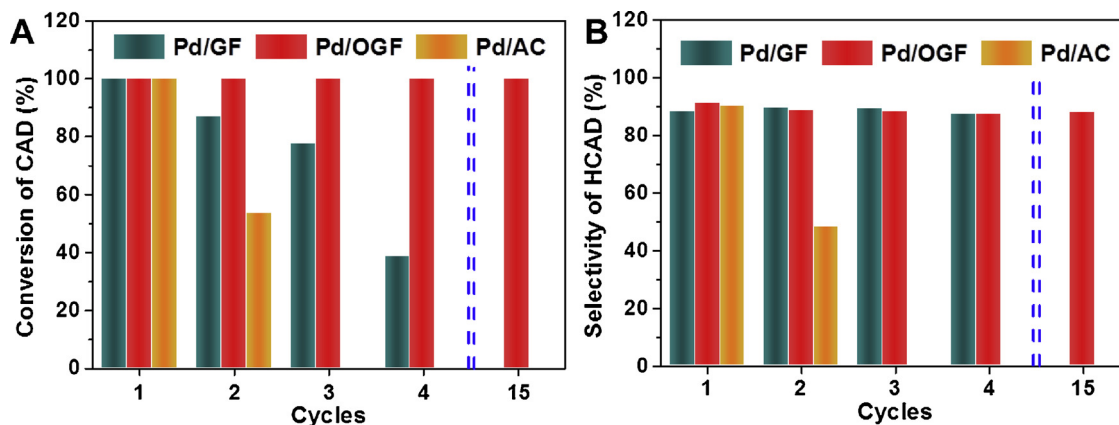

Fig. 7. (A) Cinnamaldehyde conversion and (B) C═C bond hydrogenation selectivity as a function of the cycling tests on Pd/OGF, Pd/GF and commercial Pd/AC catalysts. Conditions: 80 °C, 50 mL/min H_2, 1 atm, 375 rpm and 0.08 mol/L of CAD.

removal of the supernatant liquid followed by two consecutive washing steps. The efficiency of the washing step was controlled by analyzing the solution by GC to determine if any reactant or product remains in the washing solution. The catalytic performance under the reference conditions (50 mL/min H_2, 80 °C, 1 atm, 375 rpm, and 0.08 mol/L of CAD), expressed in terms of the conversion of CAD and selectivity of HCAD, as a function of cycling tests is presented in Fig. 7A and B, respectively.

The Pd/OGF catalyst displays an extremely high stability as no deactivation is observed even after up to 15 cycling tests (Fig. 7A). On the contrary, the commercial Pd/AC catalyst shows a drastic hydrogenation activity loss as only 50% of conversion is retained after the second test. The untreated Pd/GF catalyst displays a high

hydrogenation activity at the beginning followed by a gradual but slower deactivation, compared to that observed for the commercial powdered Pd/AC catalyst, as a function of cycling tests. However, after fourth cycles only 40% of the initial hydrogenation activity was retained on the Pd/GF catalyst which indicates that severe deactivation has occurred. The catalyst stability of Pd/OGF was further demonstrated under low conversion, as shown in Figure S6, the conversion of CAD over Pd/OGF still remain at 22% along with the HCAD selectivity of 90% during the fifteen cycling tests. It is worthy to note that a significant selectivity loss on the commercial powder catalyst was observed after only two cycles, but on the contrary, the selectivity towards HCAD on both structured catalysts remains unchanged as a function of cycling tests (Fig. 7B).
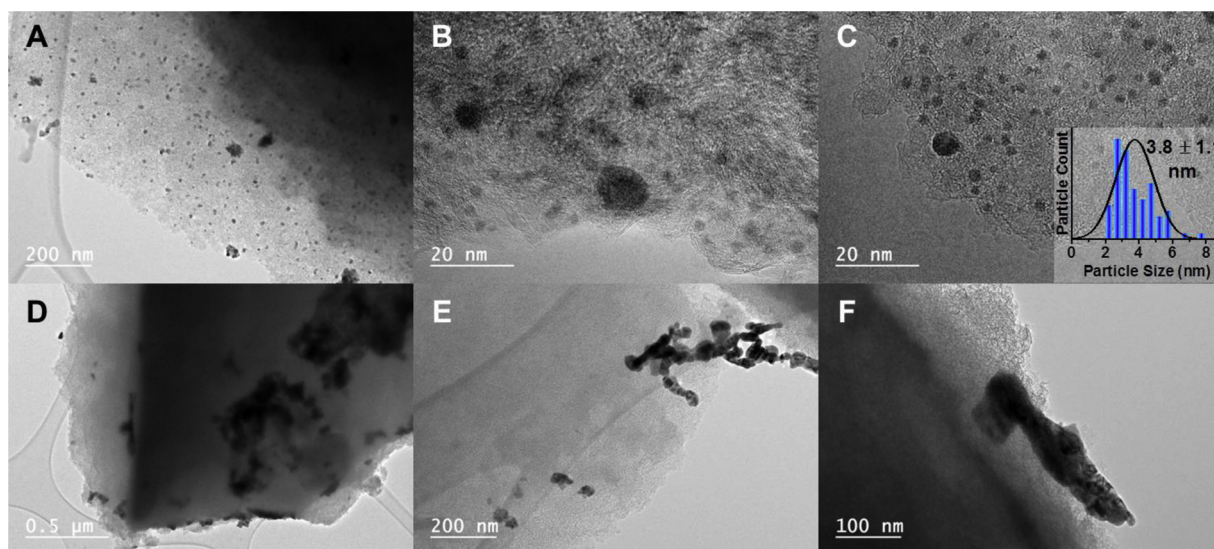
Fig. 8. TEM images of the spent Pd/OGF (A, B, C) after 15 cycling tests and Pd/GF (D, E, F) after 4 cycling tests.

TEM analysis was carried out on the spent Pd/GF and Pd/OGF and the results are displayed in Fig. 8 and Table 2. The palladium particles on the Pd/OGF, after fifteen cycling tests, remain high dispersion with a similar particle size as that observed for the freshly reduced catalyst (Fig. 8A–C). The Pd particle size distribution (Fig. 8C inset) determined from more than 200 particles remains at around 3.8 nm which is similar to that of the freshly reduced catalyst. On the other hand, there was a dramatic change for the Pd particle size on the Pd/GF after only 4 cycling tests where Pd particles assembled in large aggregates were observed (Fig. 8D–F and Table 2). These data suggest that the aggregation or sintering of metal particles was the key factor contributing to the deactivation of Pd/GF catalyst during the cycling tests. Indeed, on such structured catalyst the catalyst loss during the recovery step is unlikely occurs. The sintering phenomenon observed could be attributed to the low metal-support interactions, i.e. lack of defects and oxygenated functional groups, compared to that of the OGF support. It is expected that the sintering of Pd NPs on the Pd/GF catalyst is at the origin of the lower hydrogen dissociative adsorption on the catalyst as mentioned before, which results in the hydrogenation activity loss with cycling tests while maintaining the C=C hydrogenation bond selectivity. Such phenomenon could also happen to the deactivated Pd/AC powdered catalyst. On the other hand, the striking selectivity loss of this powdered catalyst pointed out the important variation on the catalyst nature, i.e. microstructural change. Indeed, the slurry suspension of powder catalysts suffers from the inevitable attrition of solid particles under vigorous stirring during the test, and then the finer powders formed could led to a troublesome mass transfer of the hydrogenated intermediate product in the porosity, which could induce longer sojourn time leading to over-hydrogenation before escaping [59]. Besides, as shown in Figure S7, compared with powdery samples, the structured catalysts also exhibit easier catalyst-product recovery which represents an important parameter for operating liquid-phase reactions.

The leaching test (SI Section S8) suggests the almost negligible leaching of active metal on Pd/OGF catalyst, thus confirming the strong metal-support interaction, which helps not only the Pd dispersion and stability against sintering but also its anchorage. The catalyst was compared with other reported Pd-based catalysts in hydrogenation of cinnamaldehyde and the different catalytic results are summarized in Table S1. The Pd/OGF catalyst shows a relatively high catalytic activity and stability as well as recyclability compared to the other monolith or powder catalysts operated at lower cycling tests, which could be attributed to the strong metal-support interaction to prevent active phase sintering or leaching. Combined with the easier catalyst-product

recovery of structured catalyst in the liquid-phase process, these results pointed out the high efficiency of the monolith Pd/OGF catalyst to perform liquid-phase hydrogenation of cinnamaldehyde.

4. Conclusion

In summary, using a simple gaseous acid treatment we succeeded in the synthesis of a novel structured catalyst support with high anchorage sites through defects and oxygenated functional groups from commercial graphite felt raw material. Such support displays strong interaction with the deposited metal NPs which showed excellent catalytic activity and stability as well as recyclability through an easy recovery in liquid-phase hydrogenation of cinnamaldehyde. It is demonstrated that the charge transfer at Pd-support interface can be induced by the oxygen functionalization of GF. The partial positively charged metal phase $Pd^{\delta\delta+}$, because of the electron transfer from Pd atoms to the OGF through oxygenated functional groups decorating defects, are responsible for both anchoring and stabilization of Pd NPs, which ultimately account for the enhanced resistance of Pd/OGF to sintering and/or aggregation during both catalyst preparation and cycling tests. The as-synthesized Pd/OGF catalyst displays high hydrogenation activity even at low hydrogen rate supply and high reactant concentration along with high stability with cycling tests. In addition, it is expected that the stabilization of metal NPs on oxygen functionalized carbon supports via the charge-transfer mechanism is not limited to the Pd/OGF system, but can be extended further and made applicable to other carbon supported metal systems. Work is ongoing to evaluate such metal/oxidized carbon catalyst, in other gas-phase reactions, i.e. CO_2 methanation, where highly dispersed metal NPs with good thermal stability play a vital role for catalytic performance.

Appendix A. Supplementary data

Supplementary material related to this article can be found, in the online version, at doi:https://doi.org/10.1016/j.apcatb.2018.11.041.

References

[1] P. Lanzafame, S. Perathoner, G. Centi, S. Gross, E.J.M. Hensen, Grand challenges for catalysis in the science and technology roadmap on catalysis for Europe: moving ahead for a sustainable future, Catal. Sci. Technol. 7 (2017) 5182–5194.

[2] M. Beller, G. Centi, L. Sun, Chemistry future: priorities and opportunities from the sustainability perspective, ChemSusChem 10 (2017) 6–13.

[3] S.C. Tsang, V. Caps, I. Paraskevas, D. Chadwick, D. Thompsett, Magnetically separable, carbon-supported nanocatalysts for the manufacture of fine chemicals, Angew. Chem. Int. Ed. 116 (2001) 5763–5767.

[4] W. Baaziz, L. Truong-Phuoc, C. Duong-Viet, G. Melinte, I. Janowska, V. Papaefthimiou, O. Ersen, S. Zafeiratos, D. Begin, S. Begin-Colin, C. Pham-Huu, Few layer graphene decorated with homogeneous magnetic Fe$_3$O$_4$ nanoparticles with tunable covering densities, J. Mater. Chem. A 2 (2014) 2690–2700.

[5] E. García-Bordejé, I. Kvande, D. Chen, M. Rønning, Carbon Nanofibers Uniformly Grown on γ-Alumina Washcoated Cordierite Monoliths, Adv. Mater. 18 (2006) 1589–1592.

[6] S.R.Ad. Loos, Jvd. Schaaf, M.H.J.Md Croon, T.A. Nijhuis, J.C. Schouten, Heterogeneous catalysis in a microchannel using a layer of carbon nanofibers on the channel wall, Chem. Eng. J. 179 (2012) 242–252.

[7] K. Chizari, A. Deneuve, O. Ersen, I. Florea, Y. Liu, D. Edouard, I. Janowska, D. Begin, C. Pham-huu, Nitrogen-doped carbon nanotubes as a highly active metal-free catalyst for selective oxidation, ChemSusChem 5 (2012) 102–108.

[8] L. Truong-Phuoc, T. Truong-Huu, L. Nguyen-Dinh, W. Baaziz, T. Romero, D. Edouard, D. Begin, I. Janowska, C. Pham-Huu, Silicon carbide foam decorated with carbon nanofibers as catalytic stirrer in liquid-phase hydrogenation reactions, Appl. Catal. A 469 (2014) 81–88.

[9] E. Garcia-Bordejé, Y. Liu, D.S. Su, C. Pham-Huu, Hierarchically structured reactors containing nanocarbons for intensification of chemical reactions, J. Mater. Chem. A 5 (2017) 22408–22441.

[10] Y. Peng, J.T. Richardson, Properties of ceramic foam catalyst supports one-dimensional and two-dimensional heat transfer correlations, Appl. Catal. A 266 (2004) 235–244.

[11] D.S. Su, S. Perathoner, G. Centi, Nanocarbons for the Development of Advanced Catalysts, Chem. Rev. 113 (2013) 5782–5816.

[12] J.-P. Tessonnier, M. Becker, W. Xia, F. Girgsdies, R. Blume, L. Yao, D.S. Su, M. Muhler, R. Schlögl, Spinel-type cobalt–Manganese-Based mixed oxide as sacrificial catalyst for the high-yield production of homogeneous carbon nanotubes, ChemCatChem 2 (2010) 1559–1561.

[13] P. Serp, M. Corrias, P. Kalck, Carbon nanotubes and nanofibers in catalysis, Appl. Catal. A 253 (2003) 337–358.

[14] Z. Li, J. Liu, C. Xia, F. Li, Nitrogen-Functionalized Ordered Mesoporous Carbons as Multifunctional Supports of Ultrasmall Pd Nanoparticles for Hydrogenation of Phenol, ACS Catal. 3 (2013) 2440–2448.

[15] R. Nie, M. Miao, W. Du, J. Shi, Y. Liu, Z. Hou, Selective hydrogenation of C=C double bond over N-doped reduced graphene oxides supported Pd catalyst, Appl. Catal. B 180 (2016) 607–613.

[16] W. Shi, B. Zhang, Y. Lin, Q. Wang, Q. Zhang, D.S. Su, Enhanced chemoselective hydrogenation through tuning the interaction between Pt nanoparticles and carbon supports: insights from identical location transmission electron microscopy and X-ray photoelectron spectroscopy, ACS Catal. 6 (2016) 7844–7854.

[17] J. Luo, H. Wei, Yuefeng Liu, D. Zhang, B. Zhang, W. Chu, C. Pham-Huu, D.S. Su, Oxygenated group and structural defect enriched carbon nanotubes for immobilizing gold nanoparticles, Chem. Commun. 53 (2017) 12750–12753.

[18] J. Amadou, K. Chizari, M. Houllé, I. Janowska, O. Ersen, D. Bégin, C. Pham-Huu, N-doped carbon nanotubes for liquid-phase C=C bond hydrogenation, Catal. Today 138 (2008) 62–68.

[19] D. Higgins, M.A. Hoque, M.H. Seo, R. Wang, F. Hassan, J.-Y. Choi, M. Pritzker, A. Yu, J. Zhang, Z. Chen, Development and simulation of sulfur-doped graphene supported platinum with exemplary stability and activity towards oxygen reduction, Adv. Funct. Mater. 24 (2014) 4325–4336.

[20] C. Chen, X. Li, L. Wang, T. Liang, L. Wang, Y. Zhang, J. Zhang, Highly porous nitrogen- and phosphorus-codoped graphene an outstanding support for Pd catalysts to oxidize 5-Hydroxymethylfurfural into 2,5-Furandicarboxylic acid, ACS Sustain. Chem. Eng. 5 (2017) 11300–11306.

[21] M. Sun, X.-R. Ru, L.-F. Zhai, In-situ fabrication of supported iron oxides from synthetic acid mine drainage: high catalytic activities and good stabilities towards electro-Fenton reaction, Appl. Catal. B 165 (2015) 103–110.

[22] R. Vieira, C. Pham-Huu, N. Keller, M.J. Ledoux, New carbon nanofiber/graphite felt composite for use as a catalyst support for hydrazine catalytic decomposition, Chem. Commun. (2002) 954–955.

[23] J. Luo, Y. Liu, H. Wei, B. Wang, K.-H. Wu, B. Zhanga, D.S. Su, A green and economical vapor-assisted ozone treatment process for surface functionalization of carbon nanotubes, Green Chem. 19 (2017) 1052–1062.

[24] C. Duong-Viet, L. Truong-Phuoc, T. Tran-Thanh, J.-M. Nhut, L. Nguyen-Dinh, I. Janowska, D. Begin, C. Pham-Huu, Nitrogen-doped carbon nanotubes decorated silicon carbide as a metal-free catalyst for partial oxidation of H$_2$S, Appl. Catal. A 482 (2014) 397–406.

[25] C. Duong-Viet, Y. Liu, H. Ba, L. Truong-Phuoc, W. Baaziz, L. Nguyen-Dinh, J.-

[26] M. Nhut, C. Pham-Huu, Carbon nanotubes containing oxygenated decorating defects as metal-free catalyst for selective oxidation of H$_2$S, Appl. Catal. B 191 (2016) 29–41.

[27] Z. Xu, C. Duong-Viet, H. Ba, B. Li, T. Truong-Huu, L. Nguyen-Dinh, C. Pham-Huu, Gaseous nitric acid activated graphite felts as hierarchical metal-free catalyst for selective oxidation of H$_2$S, Catalysts 8 (4) (2018) 145.

[27] M.A. Leon, T.A. Nijhuis, Jvd. Schaaf, J.C. Schouten, Mass transfer modeling of a consecutive reaction in rotating foam stirrer reactors: selective hydrogenation of a functionalized alkyne, Chem. Eng. Sci. 73 (2012) 412–420.

[28] H. Yu, Q. Zhang, M. Dahl, J.B. Joo, X. Wang, L. Wang, Y. Yin, Dual-pore carbon shells for efficient removal of humic acid from, Chem. Eur. J. 23 (2017) 16249–16256.

[29] L.G. Cancado, A. Jorio, E.H.M. Ferreira, F. Stavale, C.A. Achete, R.B. Capaz, M.V.O. Moutinho, A. Lombardo, T.S. Kulmala, A.C. Ferrari, Quantifying defects in graphene via raman spectroscopy at different excitation energies, Nano Lett. 11 (2011) 3190–3196.

[30] A. Sadezky, H. Muckenhuber, H. Grothe, R. Niessner, U. Pöschl, Raman microspectroscopy of soot and related carbonaceous materials Spectral analysis and structural information, Carbon 43 (2005) 1731–1742.

[31] T.T. Thanh, H. Ba, L. Truong-Phuoc, J.-M. Nhut, O. Ersen, D. Begin, I. Janowska, D.L. Nguyen, P. Granger, C. Pham-Huu, A few-layer graphene-graphene oxide composite containing nanodiamonds as metal-free catalysts, J. Mater. Chem. A 2 (2014) 11349–11357.

[32] R. Huang, J. Xu, J. Wang, X. Sun, W. Qi, C. Liang, D.S. Su, Oxygen breaks into carbon nanotubes and abstracts hydrogen from propane, Carbon 96 (2016) 631–640.

[33] J.L. Figueiredo, Funtionalization of porous carbons for catalytic applications, J. Mater. Chem. A 1 (2013) 9351–9364.

[34] Z. Zhang, J. Xi, H. Zhou, X. Qiu, KOH etched graphite felt with improved wettability and activity for vanadium flow batteries, Electrochim. Acta 218 (2016) 15–23.

[35] O. Ersen, C. Hirlimann, M. Drillon, J. Werckmann, F. Tihay, C. Pham-Huu, C. Crucifix, P. Schultz, 3D-TEM characterization of nanometric objects, Solid State Sci. 9 (12) (2007) 1088–1098.

[36] W.-J. Shen, M. Okumura, Y. Matsumura, M. Haruta, The influence of the support on the activity and selectivity of Pd in CO hydrogenation, Appl. Catal. A 213 (2001) 225–232.

[37] C. Amorim, M.A. Keane, Palladium supported on structured and nonstructured carbon: a consideration of Pd particle size and the nature of reactive hydrogen, J. Colloid Interface Sci. 322 (1) (2008) 196–208.

[38] S. Jujjuri, M.A. Keane, Catalytic hydrodechlorination at low hydrogen partial pressures: activity and selectivity response, Chem. Eng. J. 157 (1) (2010) 121–130.

[39] R.G. Rao, R. Blume, T.W. Hansen, E. Fuentes, K. Dreyer, S. Moldovan, O. Ersen, D.D. Hibbitts, Y.J. Chabal, R. Schlögl, J.-P. Tessonnier, Interfacial charge distributions in carbon-supported palladium catalysts, Nat. Commun. 8 (2017) 340.

[40] T. Pillo, R. Zimmermann, P. Steiner, S. Hüfner, The electronic structure of PdO found by photoemission (UPS and XPS) and inverse photoemission (BIS), J. Phys. Condens. Matter 9 (1997) 3987–3999.

[41] F. Cárdenas-Lizana, Y. Hao, M. Crespo-Quesada, I. Yuranov, X. Wang, M.A. Keane, L. Kiwi-Minsker, Selective gas phase hydrogenation of p-Chloronitrobenzene over Pd catalysts: role of the support, ACS Catal. 3 (6) (2013) 1386–1396.

[42] L. Jiang, H. Gu, X. Xu, X. Yan, Selective hydrogenation of o-chloronitrobenzene (o-CNB) over supported Pt and Pd catalysts obtained by laser vaporization deposition of bulk metals, J. Mol. Catal. A Chem. 310 (1-2) (2009) 144–149.

[43] A.L. Dantas Ramos, Pd.S. Alves, D.A.G. Aranda, M. Schmal, Characterization of carbon supported palladium catalysts: inference of electronic and particle size effects using reaction probes, Appl. Catal. A 277 (1-2) (2004) 71–81.

[44] Y. Wang, Z. Rong, Y. Wang, J. Qu, Ruthenium nanoparticles loaded on functionalized graphene for liquid-phase hydrogenation of fine chemicals: comparison with carbon nanotube, J. Catal. 333 (2016) 8–16.

[45] S. He, Z.J. Shao, Y. Shu, Z. Shi, X.M. Cao, Q. Gao, P. Hu, Y. Tang, Enhancing Metal-support interactions by molybdenum carbide: an efficient strategy toward the chemoselective hydrogenation of alpha,beta-unsaturated aldehydes, Chem. Eur. J. 22 (16) (2016) 5698–5704.

[46] Y. Murata, E. Starodub, B.B. Kappes, C.V. Ciobanu, N.C. Bartelt, K.F. McCarty, S. Kodambaka, Orientation-dependent work function of graphene on Pd(111), Appl. Phys. Lett. 97 (14) (2010) 143114.

[47] G. Ramos-Sanchez, P.B. Balbuena, Interactions of platinum clusters with a graphite substrate, Phys. Chem. Chem. Phys. 15 (28) (2013) 11950–11959.

[48] K.X. Yao, X. Liu, Z. Li, C.C. Li, H.C. Zeng, Y. Han, Preparation of a Ru-nanoparticles/defective-graphene composite as a highly efficient arene-hydrogenation catalyst, ChemCatChem 4 (12) (2012) 1938–1942.

[49] X. Zhou, W. Chu, W. Sun, Y. Zhou, Y. Xue, Enhanced interaction of nickel clusters with pyridinic-N (B) doped graphene using DFT simulation, Comput. Theor. Chem. 1120 (2017) 8–16.

[50] F. Su, L. Lv, Fang Yin Lee, T. Liu, A.I. Cooper, X.S. Zhao, Thermally reduced ruthenium nanoparticles as a highly active heterogeneous catalyst for hydrogenation of monoaromatics, J. Am. Chem. Soc. 129 (2007) 14213–14223.

[51] K. Tedsree, T. Li, S. Jones, C.W. Chan, K.M. Yu, P.A. Bagot, E.A. Marquis, G.D. Smith, S.C. Tsang, Hydrogen production from formic acid decomposition at room temperature using a Ag-Pd core-shell nanocatalyst, Nat. Nanotechnol. 6 (5) (2011) 302–307.

[52] Q. Lu, X. Chen, D. Liu, C. Wu, M. Liu, H. Li, Y. Zhang, S. Yao, Synergistic electron transfer effect-based signal amplification strategy for the ultrasensitive detection of dopamine, Talanta 182 (2018) 428–432.

[53] L. Yang, D. Liu, S. Hao, F. Qu, R. Ge, Y. Ma, G. Du, A.M. Asiri, L. Chen, X. Sun, Topotactic conversion of alpha-Fe$_2$O$_3$ nanowires into FeP as a superior fluorosensor

for nucleic acid detection: insights from experiment and theory, Anal. Chem. 89 (4) (2017) 2191–2195.

[54] Y. Li, Y. Hu, Y. Zhao, G. Shi, L. Deng, Y. Hou, L. Qu, An electrochemical avenue to green-luminescent graphene quantum dots as potential electron-acceptors for photovoltaics, Adv. Mater. 23 (6) (2011) 776–780.

[55] G. Liao, S. Chen, X. Quan, H. Yu, H. Zhao, Graphene oxide modified g-C$_3$N$_4$ hybrid with enhanced photocatalytic capability under visible light irradiation, J. Mater. Chem. 22 (6) (2012) 2721–2726.

[56] K.P. Loh, Q. Bao, P.K. Ang, J. Yang, The chemistry of graphene, J. Mater. Chem. 20 (2010) 2277–2289.

[57] R. Tschentscher, T.A. Nijhuis, Jvd. Schaaf, B.F.M. Kuster, J.C. Schouten, Gas–liquid mass transfer in rotating solid foam reactors, Chem. Eng. Sci. 65 (2010) 472–479.

[58] C. Mu, K. Huang, T. Cheng, H. Wang, H. Yu, F. Peng, Ni foams decorated with carbon nanotubes as catalytic stirrers for aerobic oxidation of cumene, Chem. Eng. J. 306 (2016) 806–815.

[59] C. Pham-Huu, N. Keller, M.J. Ledoux, L.J. Charbonniere, R. Ziessel, Carbon nano-fiber supported palladium catalyst for liquid-phase reactions. An active and selective catalyst for hydrogenation of C=C bonds, Chem. Commun. 19 (2000) 1871–1872.